

Similarity and dynamic similarity models for large eddy simulations of a rotating convection-driven dynamo

Qiaoning Chen

Institute of Geophysics and Planetary Physics, University of California

Los Angeles, CA 90095, USA

Chris A. Jones

Department of Applied Mathematics, University of Leeds, Leeds LS2 9JT, UK

June 20, 2007

Abstract

Numerical simulations of rotating convection-driven dynamo have been found very useful to understand the inner workings of geodynamo. Parametrization of small-scale processes can allow the simulations to approach a more realistic parameter range provided that these processes are modelled properly. In line with this effort, two turbulent models, the scale-similar model of Bardina *et al.* and a dynamic similarity model, have been applied to a rotating convection-driven plane-layer dynamo simulation with an infinite Pr number in this paper. The results from the similarity model are satisfactory: the large-scale magnetic/kinetic energies and *r.m.s* magnetic/velocity field fluctuations are in much better agreement with the highly-resolved solution than with the low resolution direct simulation. The model is found to be much less sensitive to the filter scale than the *a priori* test. Implementation of a dynamic procedure to the similarity model gives better agreement provided that the two filtering scales are properly chosen. Effect of aspect ratio on the performance of the models is also studied by carrying out simulations with aspect ratio 1 and 2. The results show that performances of the models are not influenced by the aspect ratio chosen. The

low resolution direct numerical simulation suffers great numerical instability as the aspect ratio increases. **Keywords:** dynamo theory, magnetoconvection, geomagnetism, large-eddy simulations.

1 Introduction

Convection in the Earth's fluid core is a rather complicated dynamical process, involving a wide range of length and time scales. Fully resolving all the relevant scales is beyond the capability of present day computers. Although still limited, understanding of geodynamo processes has been greatly advanced during the past decade through numerous numerical simulations (Glatzmaier and Roberts, 1995; Kageyama *et al.*, 1995; Kuang and Bloxham, 1997; Kida *et al.*, 1997; Busse *et al.*, 1998; Christensen *et al.*, 1999; Sakura and Kono, 1999; etc.). Implicit in almost all of these simulations is the assumption that small-scale core turbulence is homogenous and isotropic. For instance, the subgrid-scale (SGS) stress is commonly assumed to be proportional to the large-scale rate of strain tensor, with a turbulent eddy diffusivity playing the role of the kinematic viscosity. Occasionally, hyperdiffusivity is invoked as well, in order to prevent numerical instabilities arising from inadequate numerical resolution of the small scales. Although this hyperdiffusivity may be anisotropic, as in Glatzmaier and Roberts (1995), the anisotropy is dictated by computational convenience rather than physical necessity; see also Jones and Roberts (2005). It can be cogently argued that Coriolis and Lorentz forces strongly influence the SGS, and that therefore core turbulence is very far from being isotropic; see Braginsky and Meytlis (1990), Shimizu and Loper (1997), Matsushima *et al.* (1999). This suggests, for instance, that a scalar proportionality of the SGS stress tensor and the large-scale rate of strain tensor is too simplistic, and a relationship involving a tensor eddy diffusivity might be more realistic; see e.g., Phillips and Ivers (2001, 2003); Donald and Roberts (2004). There is also some possibility that inverse cascade processes are significant, e.g., Frisch *et al.* (1975) and Pouquet *et al.* (1976).

The numerical study of rotating magnetoconvection by Buffett (2000) demonstrated substantial anisotropies in the SGS heat and momentum fluxes. He showed that the similarity model of Bardina *et al.* (1980) automatically recognized such anisotropies, while avoiding the introduction of *ad hoc* scalar eddy diffusivities that were in any case incapable of representing the fluxes adequately. The promising potential of the similarity model was confirmed by the later simulation of Matsui and Buffett (2005) of a rotating convection-driven planar dynamo, a system that we also study here. Our study differs from theirs in two main respects, however. First, we employ the original similarity model rather than the related ‘nonlinear gradient model’ (Leonard, 1974) used in their calculation. Although the original similarity model has been extensively studied in nonmagnetic turbulent flows and it was found that it cannot alone provide adequate dissipation at resolved scales (Meneveau and Katz, 2000), no study of this model in a convection-driven dynamo has been done. Second, we explore a dynamically modified similarity model, in which dynamical arguments are used to continually adjust the values of parameters that were assumed to take constant values in the original similarity model.

2 Problem formulation

2.1 A mathematical dynamo model

One simple mathematical model with which to study the geodynamo process is the plane layer dynamo, in which incompressible, electrically conducting fluid, surrounded by an electrical insulator, is confined between two infinite horizontal planes and is heated from below; it rotates at a constant angular velocity $\boldsymbol{\Omega}$ in the direction opposite to the gravitational acceleration $\mathbf{g} = -g\mathbf{e}_z$ and under certain circumstances can regenerate magnetic field \mathbf{B} . This model was first investigated by Childress and Soward (1972) who showed it capable of generating magnetic field; see also Soward (1974), Fautrelle and Childress (1982), Meneguzzi and Pouquet (1989), St. Pierre (1994), Jones and Roberts (2000), and Rotvig and Jones (2002). Apart from its geometry, the model has all the major ingredients necessary to represent the geodynamo: convection,

rotation and a self-sustained magnetic field but, because of its geometry, it is comparatively simple, making it an attractive tool with which to study the fundamental physical processes underlying the geodynamo mechanism.

For the length and time scales of principal interest, the inertial forces in the Earth's core are negligible compared with the Coriolis force. Inertial forces will therefore be ignored. The resulting Boussinesq equations, in dimensionless form, are

$$\mathbf{e}_z \times \mathbf{v} = -\nabla p + (\nabla \times \mathbf{B}) \times \mathbf{B} + qRa\mathbf{e}_z T + Ek\nabla^2 \mathbf{v}, \quad (1)$$

$$\frac{\partial \mathbf{B}}{\partial t} = \nabla \times (\mathbf{v} \times \mathbf{B}) + \nabla^2 \mathbf{B}, \quad (2)$$

$$\frac{\partial T}{\partial t} + \mathbf{v} \cdot \nabla T = q\nabla^2 T + v_z, \quad (3)$$

$$\nabla \cdot \mathbf{v} = 0, \quad \nabla \cdot \mathbf{B} = 0, \quad (4)$$

where, \mathbf{v} , \mathbf{B} and T are the dimensionless velocity, magnetic field and temperature fluctuation, respectively. The dimensionless t is in units of the magnetic diffusion time and v_z is the vertical component of the velocity \mathbf{v} . The characteristic scales used to nondimensionalize the system are the time scale d^2/η , the length scale d (the depth of the fluid layer), the velocity scale η/d , the magnetic field scale $\sqrt{(2\Omega\mu_0\rho\eta)}$, the temperature scale $\bar{\beta}d$ and the pressure scale $2\rho_0\Omega\eta$. Here η is the magnetic diffusivity and $\bar{\beta}$ is the imposed temperature gradient. The dimensionless parameters used in the calculation are named and listed in Table 1.

2.2 Large-eddy simulation and subgrid-scale models

One way to parameterize the dynamo governed by (1), (2) and (3) is to use a large-eddy (LES) simulation technique in which the large scales are directly calculated and the effects of the subgrid-scales (SGS) on the large scales must be modelled. In the LES approach, the large-scale velocity $\bar{\mathbf{v}}$ is obtained by convolution, through a spatial filter function $G_\Delta(r, x)$ (Leonard, 1974):

$$\bar{\mathbf{v}}(\mathbf{x}, t) = \int G_\Delta(\mathbf{x} - \mathbf{r})\mathbf{v}(\mathbf{r}, t)d\mathbf{r}, \quad (5)$$

where Δ is the filter width. Here we use the Gaussian filter,

$$G_\Delta(\mathbf{x}) = \sqrt{\frac{6}{\pi}} \frac{1}{\Delta} \exp\left(-\frac{6\mathbf{x}^2}{\Delta^2}\right), \quad (6)$$

noting that with this choice filtering twice at filter widths Δ and λ is equivalent to a single filter with width $\sqrt{\Delta^2 + \lambda^2}$. In this way, the velocity $\mathbf{v}(\mathbf{x}, t)$ is decomposed into a large-scale (or resolved) part $\bar{\mathbf{v}}$ and a subgrid (or unresolved) part \mathbf{v}' as $\mathbf{v} = \bar{\mathbf{v}} + \mathbf{v}'$. The magnetic field, the temperature field and any other quantity can be decomposed in a similar way. After applying the filtering operation to (1), (2) and (3), we arrive at a complete description of the LES representation of the resolved quantities:

$$\mathbf{e}_z \times \bar{\mathbf{v}} = -\nabla \bar{p} + (\nabla \times \bar{\mathbf{B}}) \times \bar{\mathbf{B}} + \nabla \cdot \boldsymbol{\tau}^{Max} + qRa\bar{T}\mathbf{e}_z + Ek\nabla^2\bar{\mathbf{v}}, \quad (7)$$

$$\frac{\partial \bar{\mathbf{B}}}{\partial t} + \bar{\mathbf{v}} \cdot \nabla \bar{\mathbf{B}} = \bar{\mathbf{B}} \cdot \nabla \bar{\mathbf{v}} - \nabla \cdot \boldsymbol{\tau}^B + \nabla^2 \bar{\mathbf{B}}, \quad (8)$$

$$\frac{\partial \bar{T}}{\partial t} + \bar{\mathbf{v}} \cdot \nabla \bar{T} = -\nabla \cdot \mathbf{Q} + \bar{v}_z + q\nabla^2 \bar{T}, \quad (9)$$

$$\nabla \cdot \bar{\mathbf{v}} = 0, \quad \nabla \cdot \bar{\mathbf{B}} = 0. \quad (10)$$

The influence of the subgrid-scales on the resolved scales is embedded in SGS terms: the Maxwell stress tensor $\boldsymbol{\tau}^{Max} = \overline{\mathbf{B}\mathbf{B}} - \bar{\mathbf{B}}\bar{\mathbf{B}}$, the turbulent electromotive force (emf) $\boldsymbol{\tau}^B = \overline{\mathbf{v}\mathbf{B}} - \bar{\mathbf{v}}\bar{\mathbf{B}} - (\overline{\mathbf{B}\mathbf{v}} - \bar{\mathbf{B}}\bar{\mathbf{v}})$ and the heat flux $\mathbf{Q} = \overline{\mathbf{v}T} - \bar{\mathbf{v}}\bar{T}$. Notice that since the magnetic Ekman number $Ek_\eta = \eta/2\Omega d^2$ is zero (which is equivalent to infinite $Pr = Ek/Ek_\eta q$), we neglect the inertial forces and so the Maxwell stress tensor $\boldsymbol{\tau}^{Max}$ instead of the Reynolds stress tensor $\boldsymbol{\tau}$ appears in Eq.(7) where $\boldsymbol{\tau} = Ek_\eta(\overline{\mathbf{v}\mathbf{v}} - \bar{\mathbf{v}}\bar{\mathbf{v}}) - (\overline{\mathbf{B}\mathbf{B}} - \bar{\mathbf{B}}\bar{\mathbf{B}})$. The ultimate goal of LES is to model the SGS terms properly, so that the evolution equations for the resolved scales make reliable predictions.

In the scale-similarity model of Bardina *et al.* (1980), the flow structure for the scales smaller than Δ is assumed to be similar to that of the scales immediately above Δ , so that the latter provides a model for the subgrid-scale stresses. This idea was originally applied to the subgrid-scale Reynolds stress $\overline{\mathbf{v}\mathbf{v}} - \bar{\mathbf{v}}\bar{\mathbf{v}}$ but was extended to heat fluxes by Germano

(1986). Generalization to the Maxwell stresses is immediate. Below is a list of all the SGS terms modeled in this study:

1. *Maxwell stress:*

$$\boldsymbol{\tau}_{sim}^{Max} = C_{mom}(\widetilde{\mathbf{B}\mathbf{B}} - \widetilde{\mathbf{B}}\widetilde{\mathbf{B}}) \approx \overline{\mathbf{B}\mathbf{B}} - \overline{\mathbf{B}}\overline{\mathbf{B}}, \quad (11)$$

2. *Turbulent electromotive force:*

$$\boldsymbol{\tau}_{sim}^B = C_{ind}(\widetilde{\mathbf{v}\mathbf{B}} - \widetilde{\mathbf{v}}\widetilde{\mathbf{B}} - (\widetilde{\mathbf{B}\mathbf{v}} - \widetilde{\mathbf{B}}\widetilde{\mathbf{v}})) \approx \overline{\mathbf{v}\mathbf{B}} - \overline{\mathbf{v}}\overline{\mathbf{B}} - (\overline{\mathbf{B}\mathbf{v}} - \overline{\mathbf{B}}\overline{\mathbf{v}}), \quad (12)$$

3. *Heat flux:*

$$\mathbf{Q}_{sim} = C_T(\widetilde{\mathbf{v}\overline{T}} - \widetilde{\mathbf{v}}\widetilde{\overline{T}}) \approx \overline{\mathbf{v}\overline{T}} - \overline{\mathbf{v}}\overline{\overline{T}}, \quad (13)$$

where $\widetilde{}$ represents a second filtering operation at a scale λ with $\lambda/\Delta \geq 1$. For isotropic homogeneous turbulence, the C coefficients are often assumed to be constants of order unity. For comparison purpose, we call this model ‘constant- C similarity model’. In this study, we choose all three C coefficients to be 1.0 for the ‘constant- C similarity model’. Since the choice of the C coefficients is arbitrary, an alternative is also sought to avoid this random selection, a so-called “dynamic similarity model”.

The idea of combing a dynamic procedure with an existing SGS model is not new. Among the dynamic models, the dynamic Smagorinsky model is the most widely used one to describe nonhomogenous and anisotropic turbulent flows; see, for example, Germano *et al.* (1991), Sullivan and Meong (1992), Piomelli (1993) and Wong and Lilly (1994). There the Smagorinsky model coefficient is dependent on time and space so that local energy-backscatter is allowed to occur, and this is the main merit of the dynamic procedure. It was shown that adding the dynamic procedure to the similarity model dissipates more energy in the small scales than did the constant- C similarity model in a two-dimensional turbulent convection (Chen and Glatzmaier 2005). For simplicity, we illustrate the dynamic procedure with the similarity model for the temperature equation; the procedure for the equation of motion and the induction

equation is similar. On applying the filtering operator $G_\lambda(\mathbf{r}, \mathbf{x})$ to the LES equation (9), we obtain

$$\frac{\partial \widetilde{T}}{\partial t} + \widetilde{\mathbf{v}} \cdot \nabla \widetilde{T} = -\nabla \cdot \mathbf{Q}' + \widetilde{v}_z + q \nabla^2 \widetilde{T}, \quad (14)$$

where the subgrid-scale heat flux is

$$\mathbf{Q}' = \widetilde{\widetilde{T}} - \widetilde{\mathbf{v}} \widetilde{T}. \quad (15)$$

The heat fluxes at the two different filtering scales Δ and λ are related by the Germano identity (Germano 1991)

$$\mathbf{Q}' - \widetilde{\mathbf{Q}} = \widetilde{\widetilde{T}} - \widetilde{\mathbf{v}} \widetilde{T}. \quad (16)$$

We now make the key assumption of the dynamical similarity method, that is that we can use the same similarity model for \mathbf{Q}' as for \mathbf{Q} , with the same C coefficients. In general, one might expect the C coefficients to depend on the filter width, but as we see below, the assumption that these coefficients are filter width independent seems to do remarkably well. We then have

$$\mathbf{Q}'_{sim} = C_T (\widetilde{\widetilde{T}} - \widetilde{\mathbf{v}} \widetilde{T}). \quad (17)$$

Here, $\widehat{\cdot}$ denotes a third filtering operation at a scale $\widehat{\lambda}$ with $\widehat{\lambda}/\lambda \geq 1$. Since C_T is assumed independent of the filtering scale, we can assume by (16) that

$$C_T (\widetilde{\widetilde{T}} - \widetilde{\mathbf{v}} \widetilde{T} - \widetilde{\widetilde{T}} + \widetilde{\mathbf{v}} \widetilde{T}) = \widetilde{\widetilde{T}} - \widetilde{\mathbf{v}} \widetilde{T}. \quad (18)$$

One way of determining C_T is to minimizing the error between the left- and right-hand sides of (18) (Lilly 1992), so we define C_T by

$$C_T(z, t) = \frac{\langle L_i M_i \rangle}{\langle M_i M_i \rangle}, \quad (19)$$

where

$$L_i = \widetilde{\widetilde{T}} - \widetilde{\mathbf{v}}_i \widetilde{T}, \quad M_i = (\widetilde{\widetilde{T}} - \widetilde{\mathbf{v}}_i \widetilde{T} - \widetilde{\widetilde{T}} + \widetilde{\mathbf{v}}_i \widetilde{T}). \quad (20)$$

and $\langle \dots \rangle$ is the average taken over the horizontal plane, in which the flow is assumed to be homogenous. Coefficients $C_{ind} = C_{ind}(z, t)$ and $C_{mom} = C_{mom}(z, t)$ can be similarly determined.

Since the ‘constant- C similarity model’ can provide local energy backscatter while the original Smagorinsky model is purely dissipative, the philosophy behind the dynamic similarity model is different from the one underpinning the dynamic Smagorinsky model. Hopefully, the dynamic similarity model will not only continue to allow energy backscatter, preserve the anisotropy of the resolved scales, but also, through the constant re-adjustment of the model coefficients, describe the actual flow dynamics more faithfully.

3 Results and discussion

The full MHD equations (1), (2) and (3) and the LES equations (7), (8), (9) were solved by expanding the velocity and magnetic fields in toroidal, poloidal, and mean field parts (Jones and Roberts, 2000). No-slip conditions were applied at the upper and lower boundaries $z = \pm \frac{1}{2}$, which were assumed to be electrically insulating; periodicity was assumed in the horizontal directions (x, y) ($[0, 1] \times [0, 1]$). The equations were integrated using a Fourier-Chebyshev pseudo-spectral collocation scheme as described in Jones and Roberts (2000). We first present the numerical results for an aspect ratio $L/W = 1$ case where L is the fluid layer’s length or width and W is its vertical z height. The influence of aspect ratio on the performance of the SGS models will be discussed later.

We first carried out a highly-resolved simulation on a $64 \times 64 \times 24$ grid; we shall refer to this as ‘DNS(H)’. The Fourier modes in this model have wavenumbers in the range $-31 \leq \ell \leq 32$ (the truncation levels $N_x = N_y = 32$) in the x and y directions. Starting from the same initial condition as in DNS(H), several simulations with the similarity model and the dynamic model were integrated on a coarser $32 \times 32 \times 24$ grid. The filtering operations were only performed in the horizontal (x, y) plane using Gaussian filters, which is a natural choice for a pseudo-spectral method. For comparison purposes, we also integrated a low resolution model on the $32 \times 32 \times 24$ grid without SGS terms; we call this ‘DNS(L)’. All the simulations used the same working parameters: (modified) Rayleigh number $Ra = 500$, Ekman number $Ek = 10^{-3}$ and

Parameter	Symbol	Value
(modified) Rayleigh number	$Ra = g\bar{\alpha}\bar{\beta}d^2/2\Omega\kappa$	500
Ekman number	$Ek = \nu/2\Omega d^2$	0.001
Magnetic Ekman number	$Ek_\eta = \eta/2\Omega d^2$	0
Roberts number	$q = \kappa/\eta$	4
Magnetic Reynolds number*	Re_m	O(10 ²)
Elsasser number*	Λ	O(10 ²)
Reynolds number	Re	0

Table 1: Parameters in the numerical simulations. * in terms of the dimensionless variables, the magnetic Reynolds number is $Re_m = \sqrt{(|\mathbf{v}|^2)}$ and the Elsasser number is $\Lambda = |\mathbf{B}|^2$. The classic Rayleigh number is $g\bar{\alpha}\bar{\beta}d^4/\nu\kappa = Ra Ek^{-1} = 5 \times 10^5$, where κ is the thermal diffusivity and $\bar{\alpha}$ is the thermal expansion coefficient.

Roberts number $q = 4.0$. The simulations were initiated by allowing non-magnetic convection to develop fully and by then introducing a very small random magnetic field. After integrating for about 0.5 magnetic diffusion time, the magnetic fields began to saturate. The Elsasser number Λ and magnetic Reynolds number Re_m both became of order 100, indicating strong field generation (Table 1). As suggested by the large value of q , the velocity field is rather smooth compared with the turbulent magnetic field. Because the field is strongly chaotic, the statistics of the solutions were accumulated over a substantial period of 0.8 magnetic diffusion times after the magnetic fields saturated.

3.1 *A priori* tests

The scale-similarity assumption can be tested by performing *a priori* tests on the DNS(H) data. We first calculated the SGS terms directly, using only one filtering operation $\Delta = 2\Delta_x$, where

$\Delta_x = 1/64$ is the grid spacing. Then the modeled SGS terms were derived from the DNS(H) data, using (11), (12) and (13) with two filtering operations $\lambda = r\Delta$ and $\Delta = 2\Delta_x$ with all 3 C -coefficients taken to be 1; two values of r are tested: $r = 4/3$ and $r = 2$. Figures 1 – 3 compare contour plots of the directly calculated SGS terms with the modelled SGS terms in the same (x, y) plane ($z = 0.0$) at time $t = 0.95$. Clearly, the spatial distributions of the modelled SGS terms strongly resembles those of the directly calculated SGS terms, the results for $r = 4/3$ being particularly close. The vertical profiles show further that the $r = 4/3$ model gives magnitudes comparable with those of the direct calculations, while those of the $r = 2.0$ model are 2 to 3 times larger (see Fig. 4). The remainder of the SGS terms (not shown) behaved in much the same way. Clearly too great a sensitivity to the choice of filter scale would not be desirable in real time LES simulations, and the assumption that the C coefficients are all 1.0 is not working well at $\lambda = 2\Delta$. This issue will be revisited in the following LES calculations.

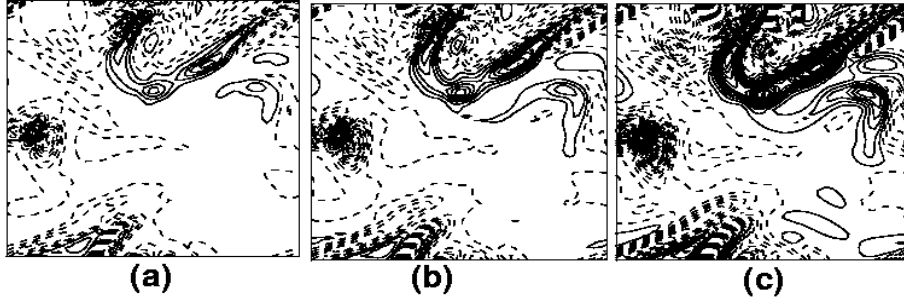


Figure 1. Contour plots of the Maxwell stress τ_{23}^{Max} from (a) direct calculations; (b) the similarity model with $\lambda = 4\Delta/3$; (c) the similarity model with $\lambda = 2\Delta$.

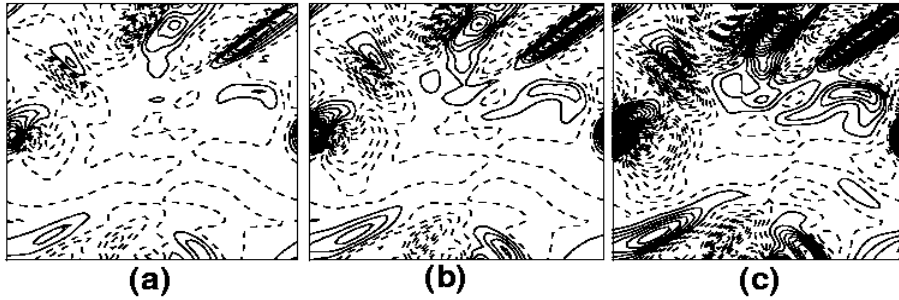


Figure 2. Contour plots of the emf component τ_{23}^B from (a) direct calculation Δ ; (b) the similarity model with $\lambda = 4\Delta/3$; (c) the similarity model with $\lambda = 2.0\Delta$.

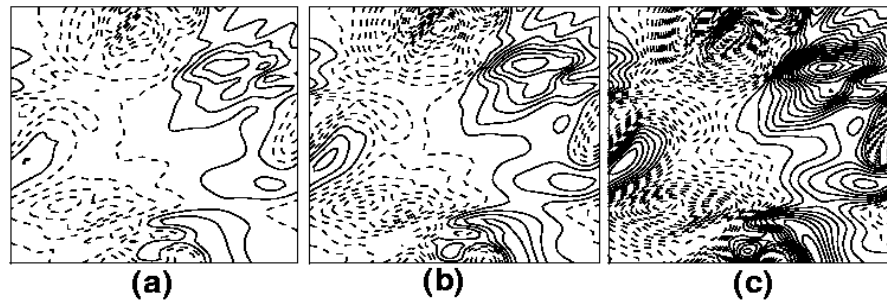


Figure 3. Contour plots of the heat flux Q_2 from (a) direct calculations; (b) the similarity model with $\lambda = 4\Delta/3$; (c) the similarity model with $\lambda = 2\Delta$.

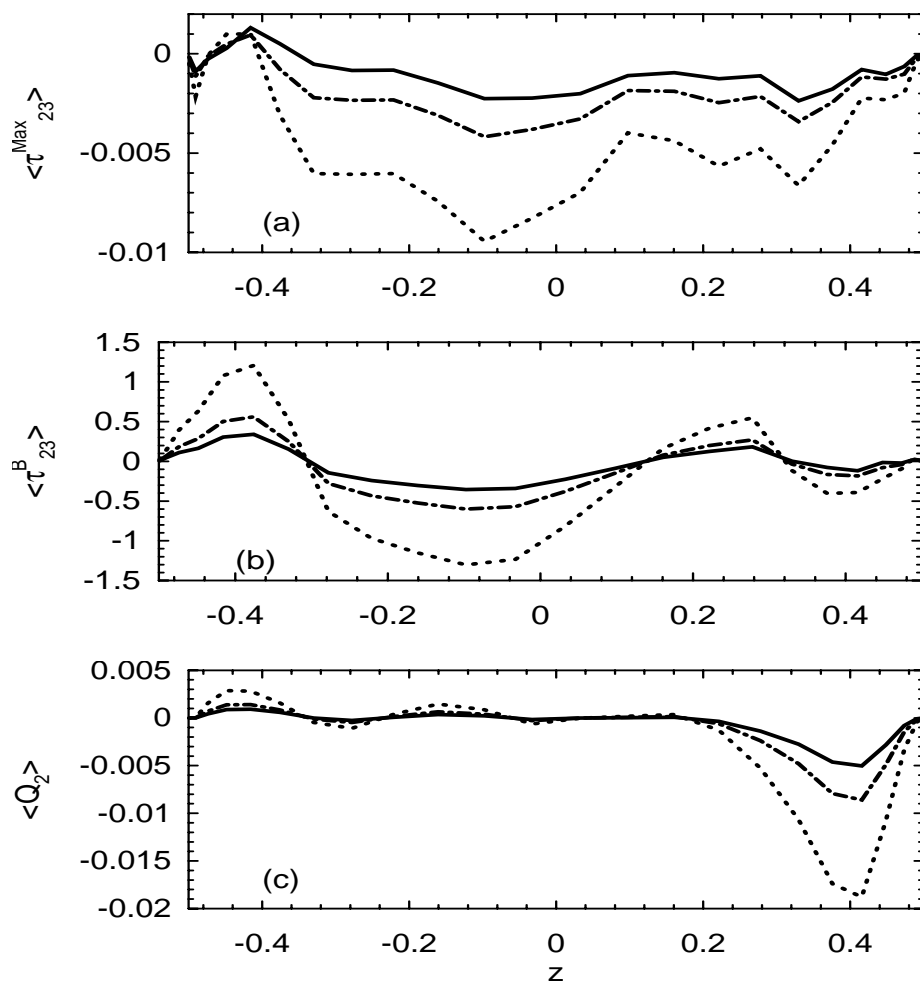


Figure 4. Vertical profiles, averaged over time and the horizontal plane, for (a) τ_{23}^{Max} ; (b) τ_{23}^B ; (c) Q_2 . Solid lines: direct calculation; $-\cdot-$: the similarity model with $\lambda = 4\Delta/3$; \dots : the similarity model with $\lambda = 2\Delta$.

3.2 The constant- C similarity models

To implement this model numerically with our pseudospectral code, we run at a certain truncation level and denote the results of (6)-(9) by $\bar{\mathbf{v}}$, \bar{B} , etc. The SGS terms are computed by applying a single filter $\tilde{\cdot}$, then supplied to the equations (7), (8) and (9) in time. Two sets of simulations were carried out for two values of λ , namely $\lambda/\Delta = 4/3$ and $\lambda/\Delta = 2$ (with Δ equal to the grid spacing) with all three C -coefficients equal to 1.0. These serve two purposes. One hopes that the statistics gathered during a sufficiently long integration time will not change dramatically from one simulation to the other from the same model. The other purpose originated from the *a priori* tests where it was observed that the SGS terms differ in magnitudes by factors of order 2–3 when there is a slight change of the filtering scale from $r = 2$ to $r = 4/3$. Will this affect the magnitude of the large-scale structures, i.e. $\bar{\mathbf{v}}$ and \bar{B} , in a real-time LES simulation? A viable model should certainly less strongly depend on the filtering scale.

It is known that flows in rapidly rotating systems deviate strongly from those in corresponding non-rotating systems. When the Coriolis force is totally dominant, the Proudman–Taylor theorem states that the flow is entirely two-dimensional with respect to the axis of rotation. A numerical study of rotating turbulence in a cubic domain (Chen *et al.*, 2005) showed further that the vertically-average (i.e., the average along the rotation axis, z) of the horizontal velocity and the vertically-averaged vertical velocity converge to two different limits as $\Omega \rightarrow \infty$. In the present study, the presence of the strong magnetic field and the buoyancy force certainly complicates this simple picture, but anisotropy and inhomogeneity must still be expected. It is natural to investigate separately the flow dynamics in planes parallel and perpendicular to the rotation axis. For this purpose, transverse and longitudinal magnetic energies are introduced,

defined by

$$E_m^\perp = E_m^{Bz} = \sum_{S(k_h)} \frac{1}{2} \langle |\bar{B}_z^f(k_h, z)|^2 \rangle_{z,t}, \quad (21)$$

$$E_m^\parallel = E_m^{Bx,By} = \sum_{S(k_h)} \frac{1}{2} \langle |\bar{B}_x^f(k_h, z)|^2 + |\bar{B}_y^f(k_h, z)|^2 \rangle_{z,t}, \quad (22)$$

respectively. Similarly, transverse and longitudinal kinetic energies are defined by

$$E_{kin}^\perp = E_{kin}^{vz} = \sum_{S(k_h)} \frac{1}{2} \langle |\bar{v}_z^f(k_h, z)|^2 \rangle_{z,t}, \quad (23)$$

$$E_{kin}^\parallel = E_{kin}^{v_x,v_y} = \sum_{S(k_h)} \frac{1}{2} \langle |\bar{v}_x^f(k_h, z)|^2 + |\bar{v}_y^f(k_h, z)|^2 \rangle_{z,t}. \quad (24)$$

Here, $\langle \dots \rangle_{z,t}$ denotes the average in the vertical and over time; $S(k_h)$ is the wave number band with central radius k_h , and \bar{B}_x^f is the Fourier mode defined by \bar{B}_x , etc.

In figure 5, spectra of the magnetic energy in the transverse and longitudinal directions are compared from the similarity models with both the DNS(H) data and the DNS(L) data. These spectra are functions of the horizontal wavenumber $k_h = \sqrt{k_x^2 + k_y^2}$ and are obtained by averaging over the z direction and over time for about 0.8 magnetic diffusion time. To do a fair comparison with the other low resolution simulations at the same large scales, the DNS(H) data is gaussian filtered at the scale $\Delta = 2\Delta_x = 2/64$. The other low resolution $32 \times 32 \times 24$ calculations, including a DNS(L) and two LES calculations from the similarity models, automatically have the results at that scale $\Delta = 1/32$. Note that the turn-up at the end, near $k_h = 15 - 16$, is a normal feature of the pseudo-spectral truncation, which for DNS(L) cuts off at $N_x = N_y = 16$. The constant C similarity model results were found by applying the filter $\lambda = 2\Delta$ and the filter $\lambda = 4/3\Delta$, separately. These LES results also show the effect of the finite truncation at $N_x = N_y = 16$. The same procedure was used to generate the kinetic energy spectra in figure 6, and the z -profiles of the time-averaged *r.m.s.* field and velocity components in figure 7.

As expected, DNS(L) generates much higher transverse and longitudinal magnetic energies than the filtered DNS(H) data. A clear improvement can be observed when the similarity model is applied with either $\lambda/\Delta = 4/3$ or $\lambda/\Delta = 2$; both LES simulations agree with DNS(H) much

better in the whole range than DNS(L). The model with $\lambda = 2\Delta$ dissipates more magnetic energy in the range $6 \leq k_h \leq 12$ than does the $\lambda = 4\Delta/3$ model. The latter seems to dissipate magnetic energy at approximately the right rate. Nevertheless, none of the simulations on the coarser grid dissipates enough energies at very small scales, $k_h = 12$ or greater. This is consistent with the findings of many large-eddy simulations of nonmagnetic turbulence. The major difference, however, is that the numerical instability commonly encountered in the non-magnetic simulations does not arise in the MHD calculations, a fact already noted by Buffett (2003). For kinetic energies, the similarity models improve the agreement with DNS(H) only for $5 \leq k_h \leq 10$ (Fig. 6). Again, the agreement with the DNS(H) model in this range is better for the $\lambda/\Delta = 4/3$ than for $\lambda/\Delta = 2$.

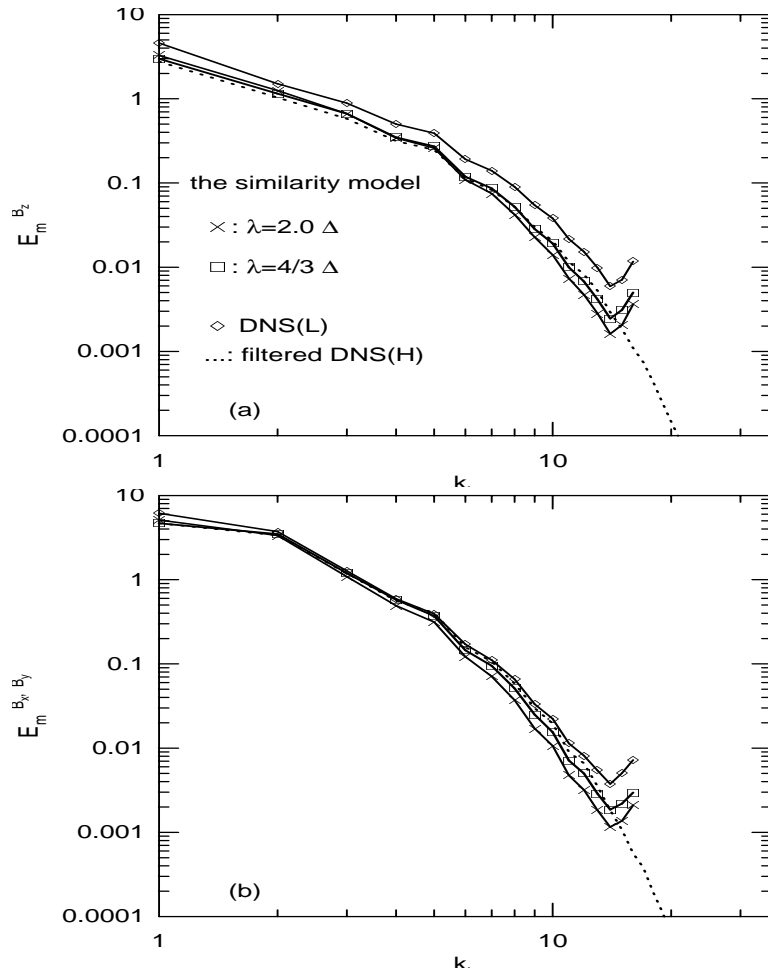


Figure 5. Time and vertically averaged spectra for (a) the transverse magnetic energy E_m^\perp ; and (b) the longitudinal magnetic energy E_m^\parallel : filtered DNS(H); \diamond : DNS(L).

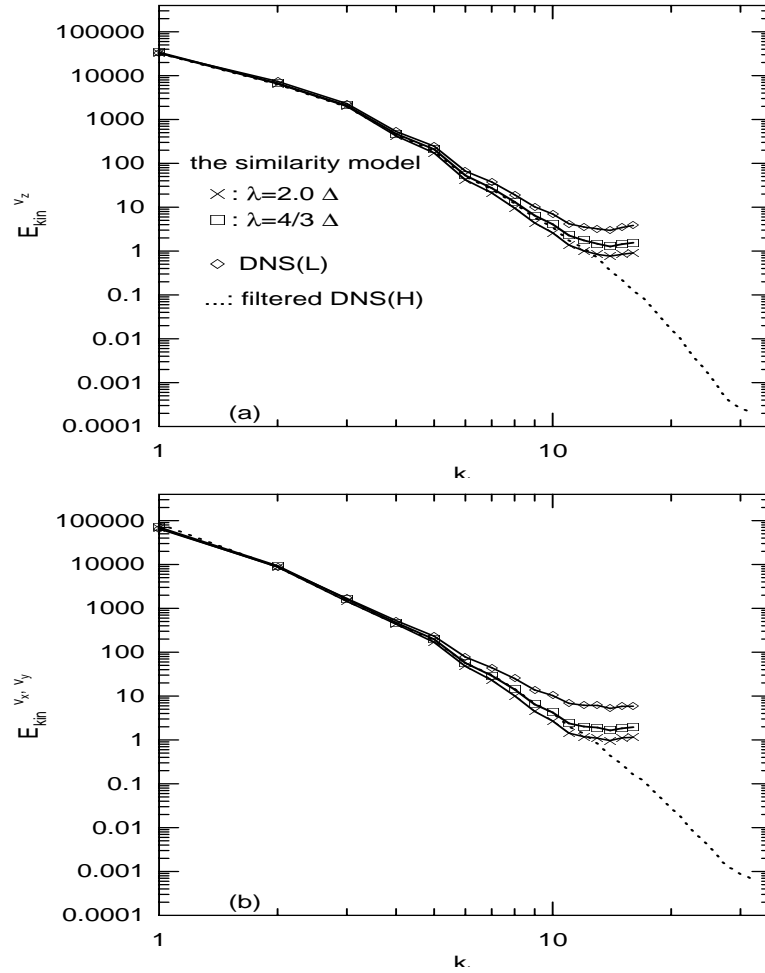


Figure 6. Time and vertically averaged spectra for (a) the transverse kinetic energy E_{kin}^\perp ; and (b) the longitudinal kinetic energy E_{kin}^\parallel : filtered DNS(H); \diamond : DNS(L).

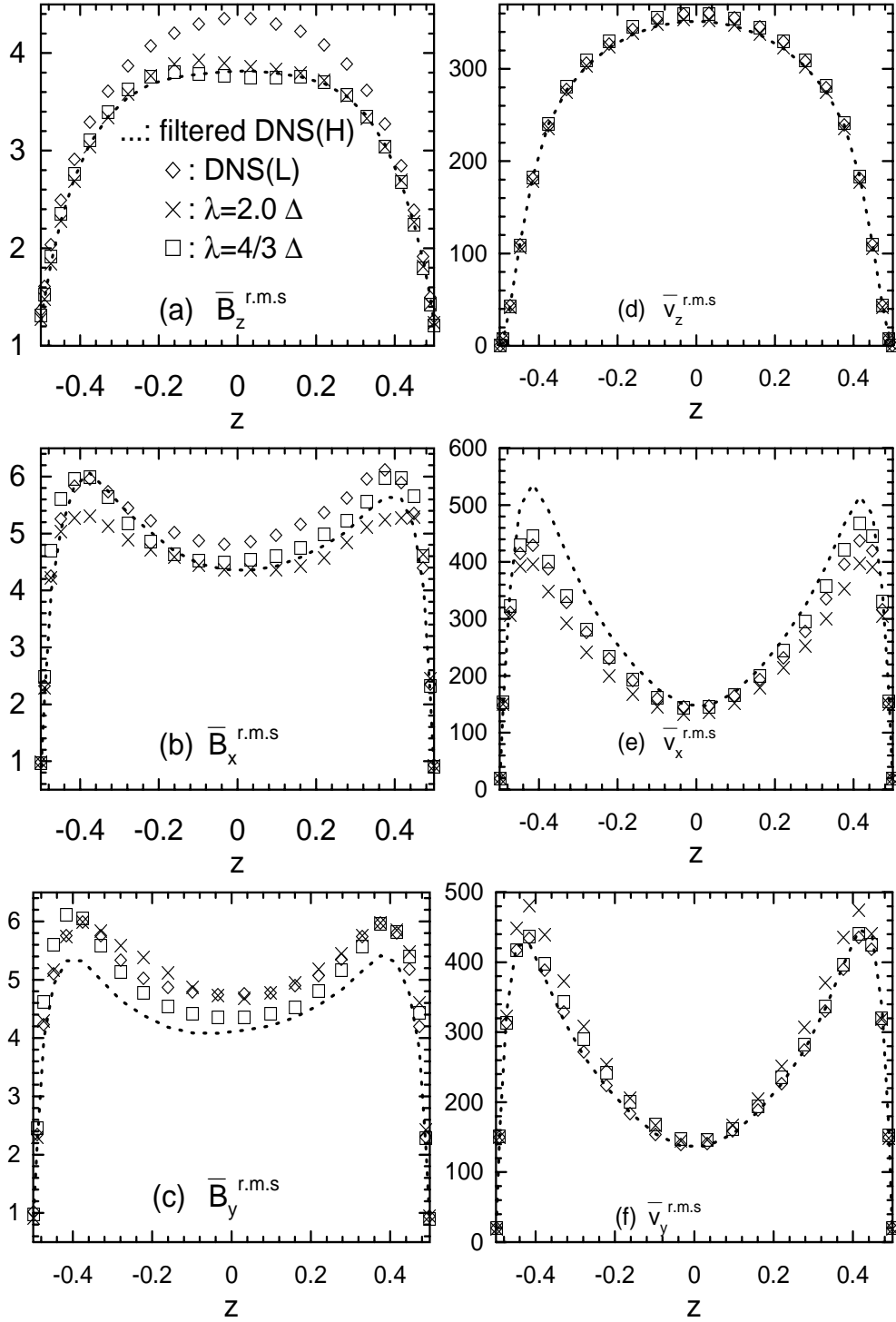


Figure 7. Vertical profiles of the time-averaged *r.m.s.* magnetic field components: (a) $\bar{B}_z^{r.m.s.}$; (b) $\bar{B}_x^{r.m.s.}$; (c) $\bar{B}_y^{r.m.s.}$; and the time-averaged *r.m.s.* velocity components: (d) $\bar{v}_z^{r.m.s.}$; (e) $\bar{v}_x^{r.m.s.}$; (f) $\bar{v}_y^{r.m.s.}$: filtered

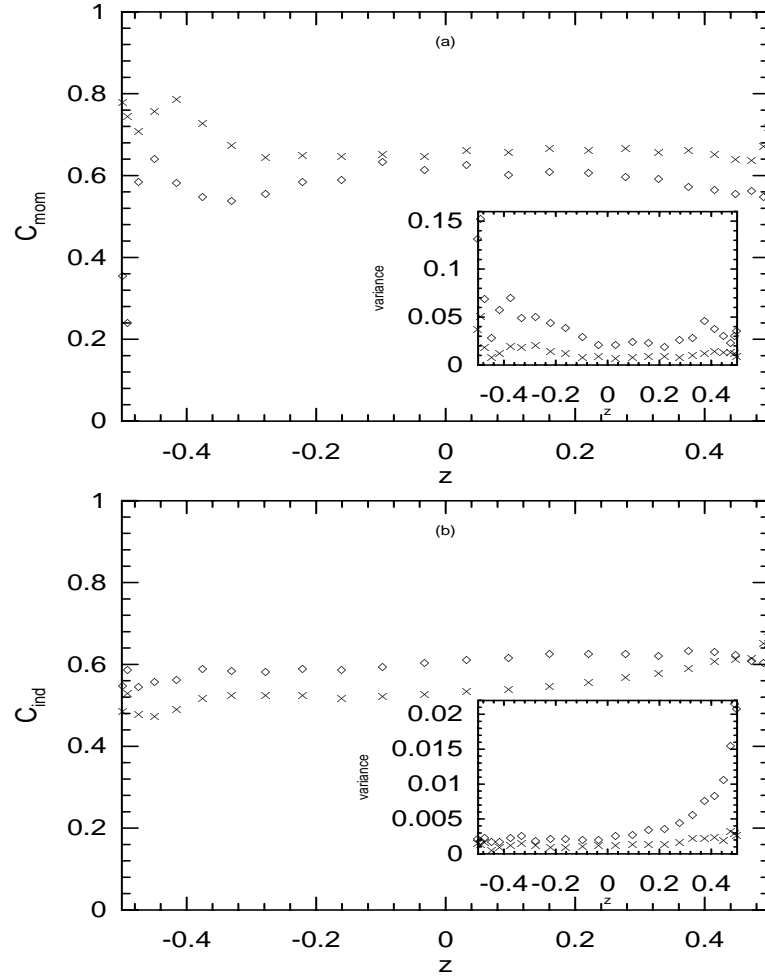
DNS(H); \diamond : DNS(L).

The left column of Fig. 7 displays magnetic field intensities measured by their root-mean-square (*r.m.s.*) fluctuations, i.e., by $\bar{B}_z^{rms} = \sqrt{\langle(\bar{B}_z - \langle\bar{B}_z\rangle)^2\rangle}$ etc. All three plots show that the similarity models agree uniformly better than DNS(L) with the filtered DNS(H). For example, \bar{B}_z^{rms} from DNS(L) is about 18% larger in magnitude than that given by the filtered DNS(H), while the increase is at most 2% from the similarity models; see Fig. 7(a). For the velocity fluctuations shown in the right column of Fig. 7, the similarity models have no obvious advantage over DNS(L). In general, we find that (1) the similarity model does give better results than DNS(L), and (2) the $\lambda = 4\Delta/3$ results are slightly superior to those from $\lambda = 2\Delta$. This is consistent with the *a priori* test, but the large-scale energy magnitudes from these two LES simulations are the same order of magnitude, obviously suggesting that the choice of the filter scale does not have a strong effect on the flow dynamics.

3.3 The dynamic similarity model

In the dynamic similarity model, the SGS terms are calculated and the coefficients are renewed constantly, therefore two parameters $\hat{\lambda}$ and λ are prescribed associated with two explicit filtering operations. Two experiments are set up using $\hat{\lambda} = 2\lambda, \lambda = 4\Delta/3$ and $\hat{\lambda} = 2\lambda, \lambda = 2\Delta$, respectively. We first show that the dynamic model is indeed capable of modifying its coefficients when the the filter scale changes. In Fig. 8 are plotted the vertical variations of the time- and horizontally-averaged coefficients for the dynamic model. These plots show that the C coefficients of the model computed as in (19) are $O(1)$, being in the range $[0.4, 0.8]$ for both $\lambda = 2\Delta$ and $\lambda = 4\Delta/3$ calculations, which is in line with the assumption in the constant- C similarity model. Interestingly, the coefficient C_{mom} is larger than C_{ind} and C_T in general. The distribution of C_T is very symmetrical, having larger values at the boundaries and smaller ones near the center; C_{ind} is almost uniformly distributed. In the inset of each figure is shown the variance of the corresponding coefficient. The variance of the model coefficient, for instance, C_T

is defined by $\sigma^2 = \langle (C_T - \langle C_T \rangle_t)^2 \rangle_t$, contains the information of how scattered the coefficient is in time. The smaller values of the variances of C_{ind} and C_T than that of C_{mom} indicates that the magnetic field fluctuates much more than velocity and temperature fields.



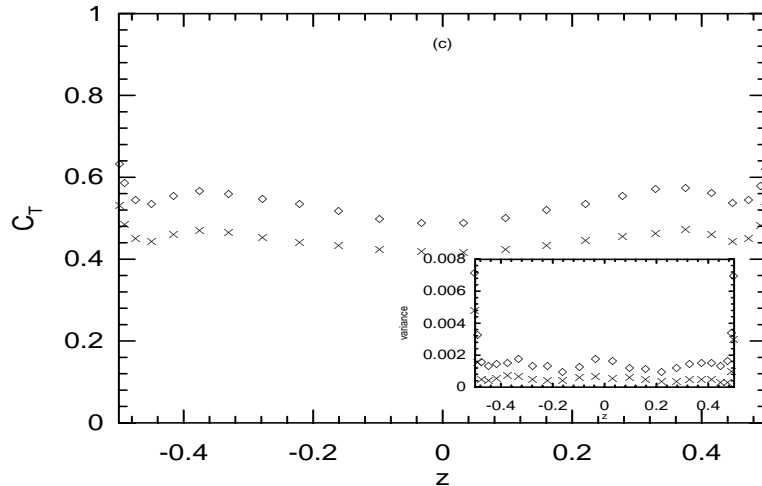


Figure 8. Vertical profiles of the time- and horizontally-averaged coefficients of the dynamic similarity model: (a) C_{mom} ; (b) C_{ind} ; (c) C_T . The insets show the corresponding variances, e.g., $\sigma^2 = \langle (C_T - \langle C_T \rangle_t)^2 \rangle_t$. (1) \diamond : $\hat{\lambda} = 2\lambda, \lambda = 2\Delta$; (2) \times : $\hat{\lambda} = 2\lambda, \lambda = 4\Delta/3$.

The comparison between the dynamic similarity model and the constant- C similarity model is shown in Fig. 9, 10, 11. The salient fact revealed by Fig. 9 is that the dynamic model not only maintains large-scale magnetic energies comparable with those of the filtered DNS(H), but also adjusts the scaling in the range $5 \leq k \leq 12$ to fit the filtered DNS(H) better. It also inherits some of the drawbacks of the similarity model with unit C -coefficients: it cannot dissipate enough energy at scales much smaller than $k \geq 12$. A similar trend can be also seen in the kinetic energy spectra (Fig. 10). The improvement of the dynamic model over the constant- C similarity models can be observed in the vertical profiles of the magnetic field intensities and velocity fluctuations; see especially Fig. 11(b),(f).

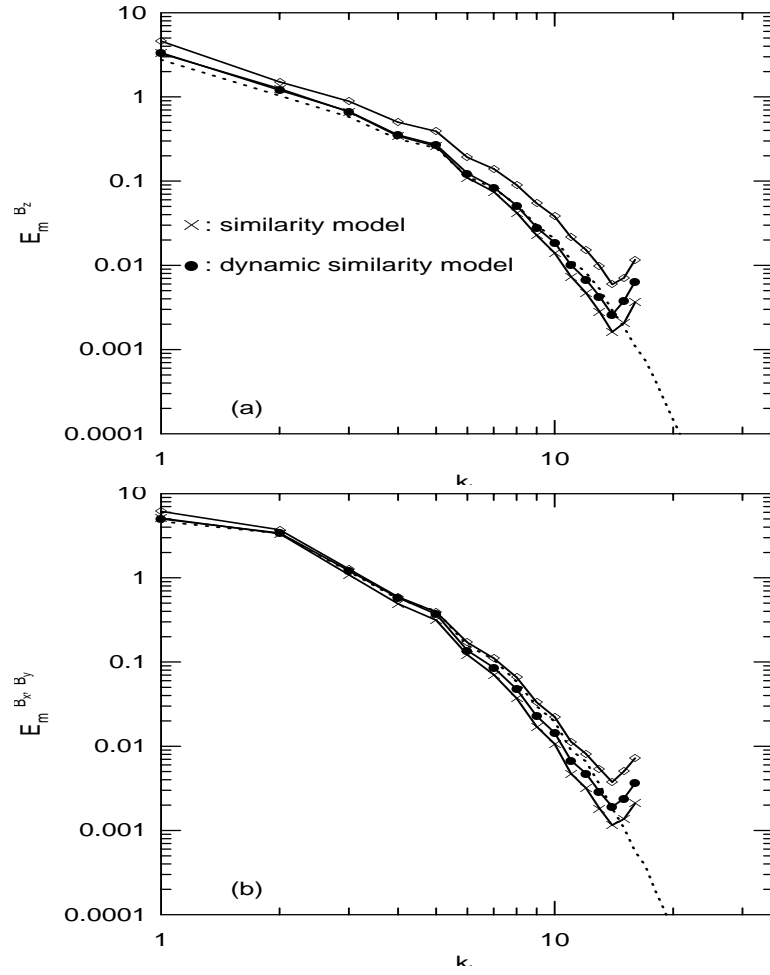


Figure 9. Time and vertically averaged spectra for (a) the transverse magnetic energy E_m^\perp ; (b) the longitudinal magnetic energy E_m^\parallel: filtered DNS(H); \diamond : DNS(L); \times : the *similarity* model with $\lambda = 2\Delta$ and $\Delta = 1/32$; \bullet : the *dynamic similarity* model with $\hat{\lambda}/\lambda = \lambda/\Delta = 2$ and $\Delta = 1/32$.

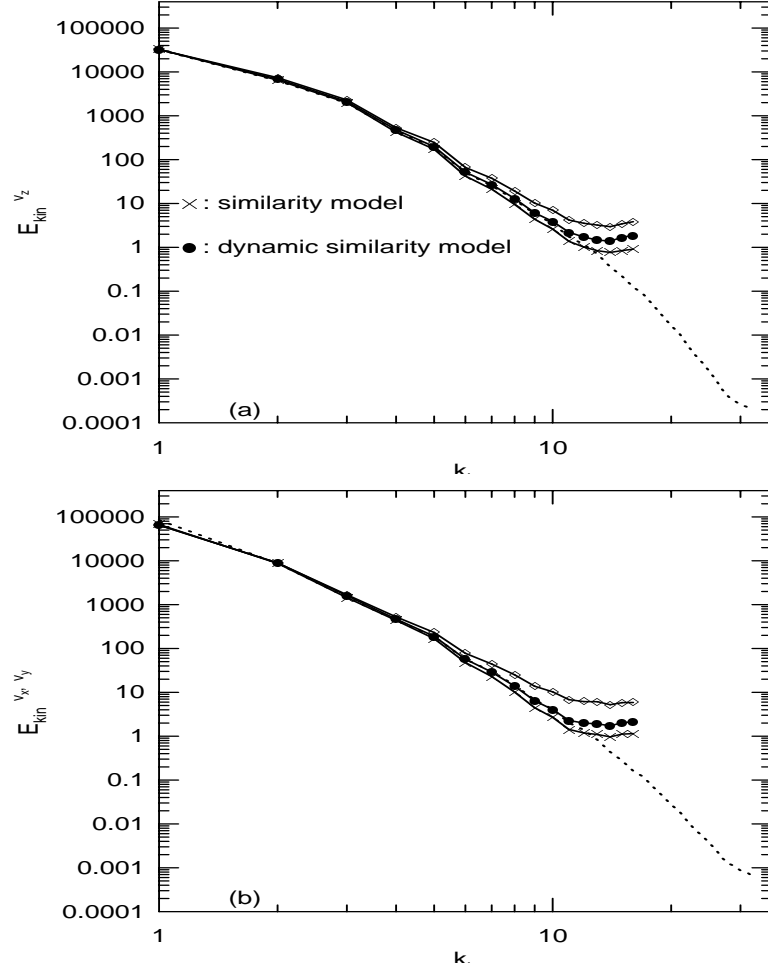


Figure 10. Time and vertically averaged spectra for (a) the transverse kinetic energy E_{kin}^{\perp} ; (b) the longitudinal kinetic energy E_{kin}^{\parallel} . \dots : filtered DNS(H); \diamond : DNS(L); \times : the *similarity* model with $\lambda = 2\Delta$; \bullet : the *dynamic similarity* model with $\hat{\lambda}/\lambda = \lambda/\Delta = 2$.

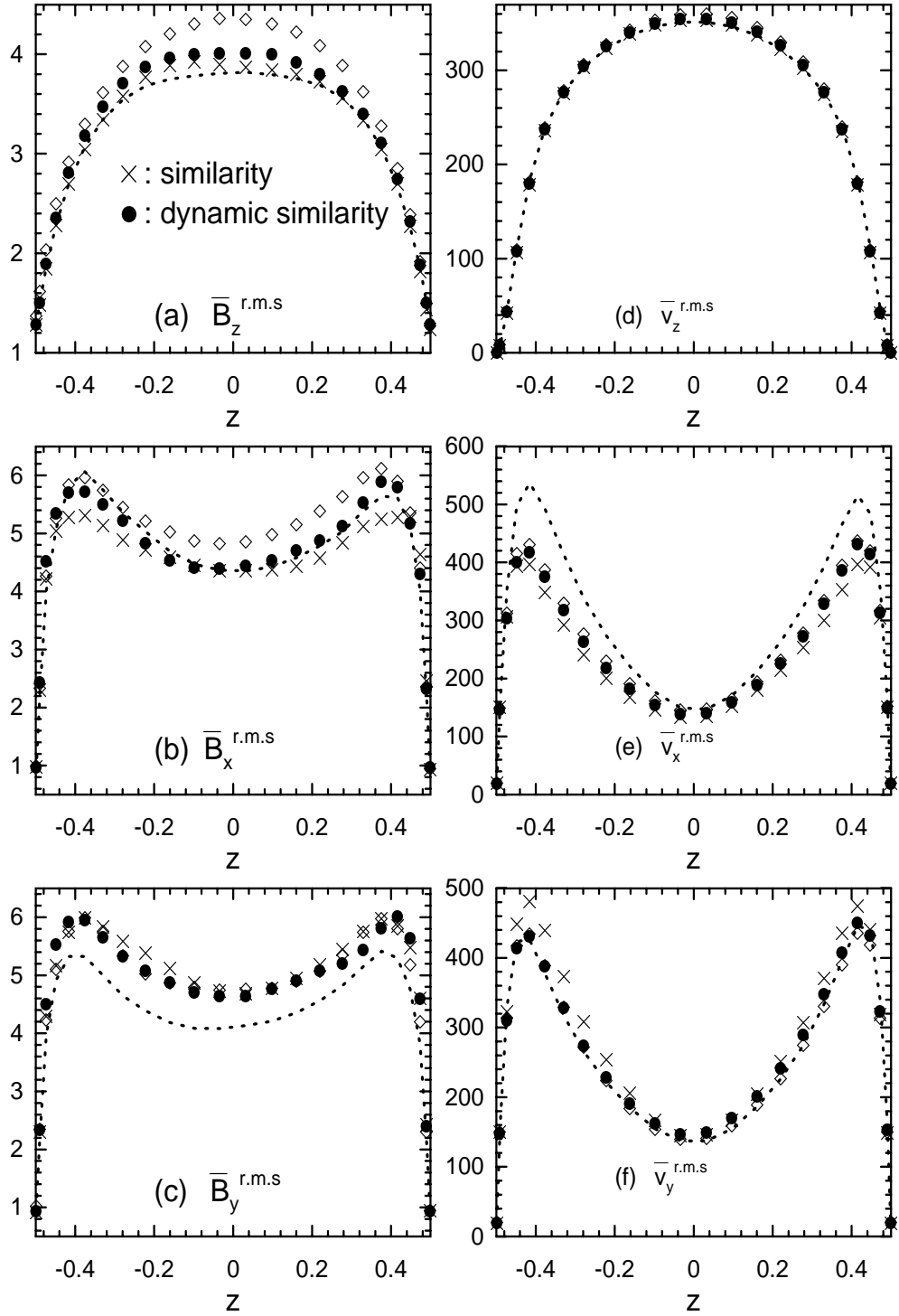


Figure 11. Vertical profiles of the time-averaged *r.m.s.* magnetic field components (a) $\bar{B}_z^{r.m.s}$; (b) $\bar{B}_x^{r.m.s}$; (c) $\bar{B}_y^{r.m.s}$; and the time-averaged *r.m.s.* velocity components: (d) $\bar{v}_z^{r.m.s}$; (e) $\bar{v}_x^{r.m.s}$; (f) $\bar{v}_y^{r.m.s}$: filtered

DNS(H); \diamond : DNS(L); \times : the *similarity* model with $\lambda = 2\Delta$; \bullet : the *dynamic similarity* model with $\hat{\lambda}/\lambda = \lambda/\Delta = 2$.

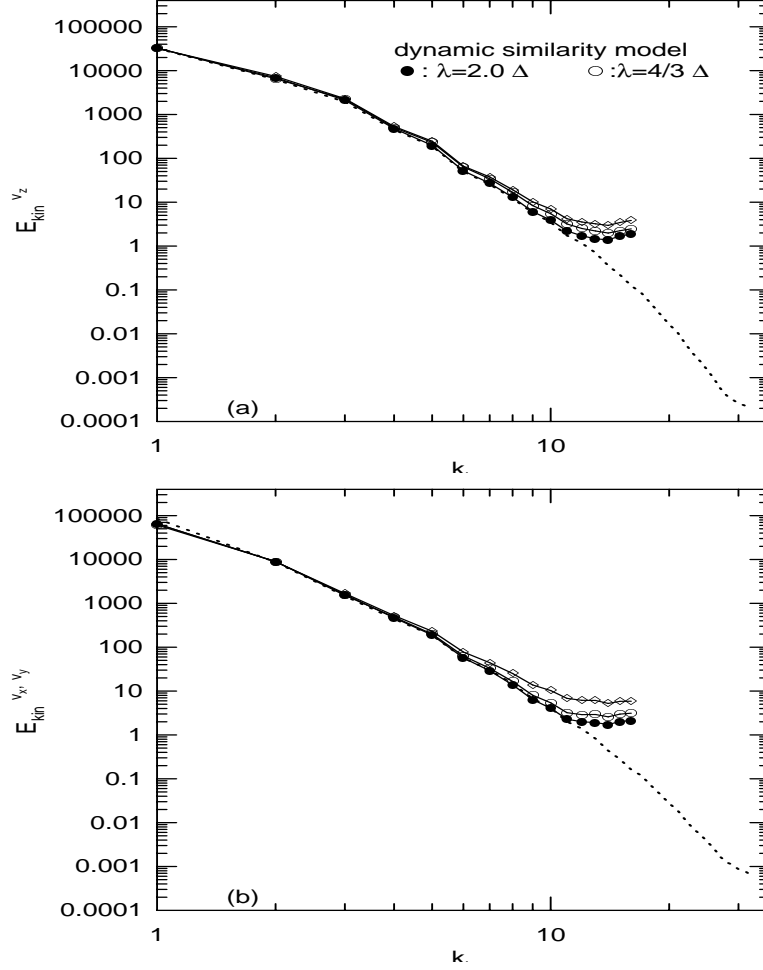
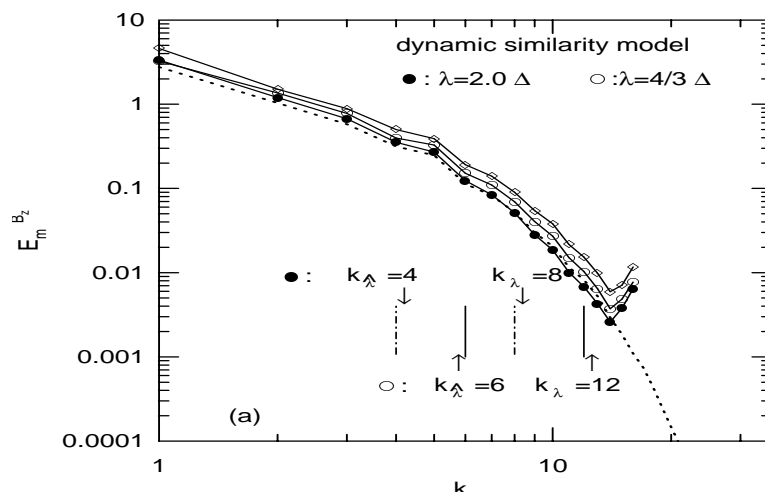


Figure 12. Time and vertically averaged spectra of (a) the transverse kinetic energy E_{kin}^{\perp} ; (b) the longitudinal kinetic energy E_{kin}^{\parallel} . \dots : filtered DNS(H); \diamond : DNS(L). $\hat{\lambda} = 2\lambda$: for both the dynamic models.

However, as we will show immediately below, because of one extra explicit filtering, the choice of $\hat{\lambda}$ complicates the problem and the results from the dynamic similarity model are not altogether satisfactory. We compared two sets of simulations using $\hat{\lambda} = 2\lambda, \lambda = 4\Delta/3$ and $\hat{\lambda} = 2\lambda, \lambda = 2\Delta$, respectively. As shown in Fig. 12 and the right column of Fig. 14, these two sets

of simulations give almost the same kinetic energy spectra and *r.m.s.* velocities. Differences are apparent in the transverse magnetic energy spectra (Fig. 12(a)) and the magnetic field intensities \bar{B}_z^{rms} and \bar{B}_x^{rms} (Fig. 13(a),(b)). The dynamic model from the choice of $\lambda = 4\Delta/3$ not only exhibits an increase of transverse magnetic energy in the scales $2 \leq k \leq 8$ seen in Fig. 13 (a), but also generates larger magnetic field intensity \bar{B}_z^{rms} in the regions $|z| \geq 0.3$ close to the boundaries, and larger magnetic field intensity \bar{B}_x^{rms} in the middle of the fluid layer. Although the difference between the two sets of LES results is not as significant as the one between DNS(H) and DNS(L), it is evident that $\lambda = 2\Delta$ is a better choice than $\lambda = 4\Delta/3$ when $\hat{\lambda} = 2\lambda$. It is not clear how these are best chosen, one possible reason is that the wavenumbers $k_{\hat{\lambda}} = 4$ and $k_{\lambda} = 8$ (corresponding to $\lambda = 2\Delta$) sample a wider range of scales than $k_{\hat{\lambda}} = 6$, $k_{\lambda} = 12$ (corresponding to $\lambda = 4\Delta/3$); see Fig. 13 (a).



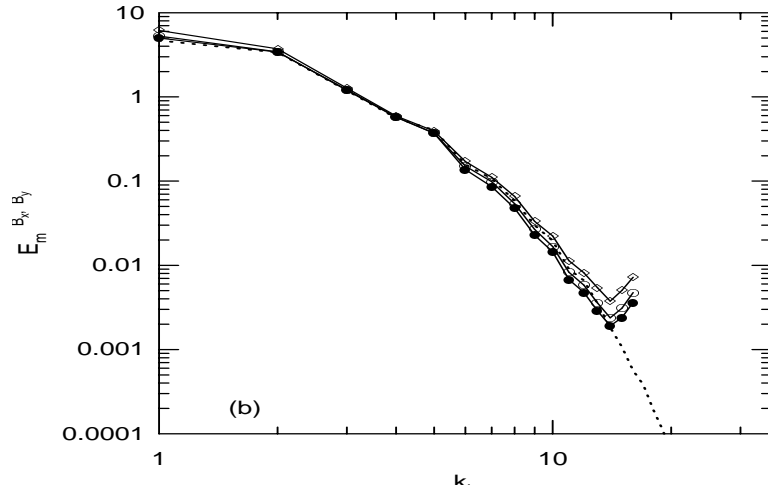
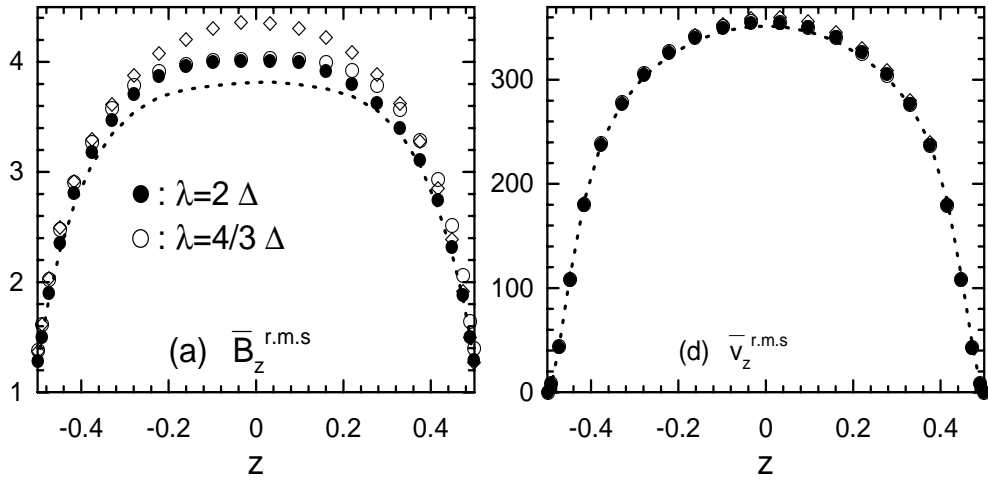


Figure 13. Time and vertically averaged spectra of (a) the transverse magnetic energy; (b) the longitudinal magnetic energy. \dots : filtered DNS(H); \diamond : DNS(L). $\hat{\lambda} = 2\lambda$ for both the dynamic models.



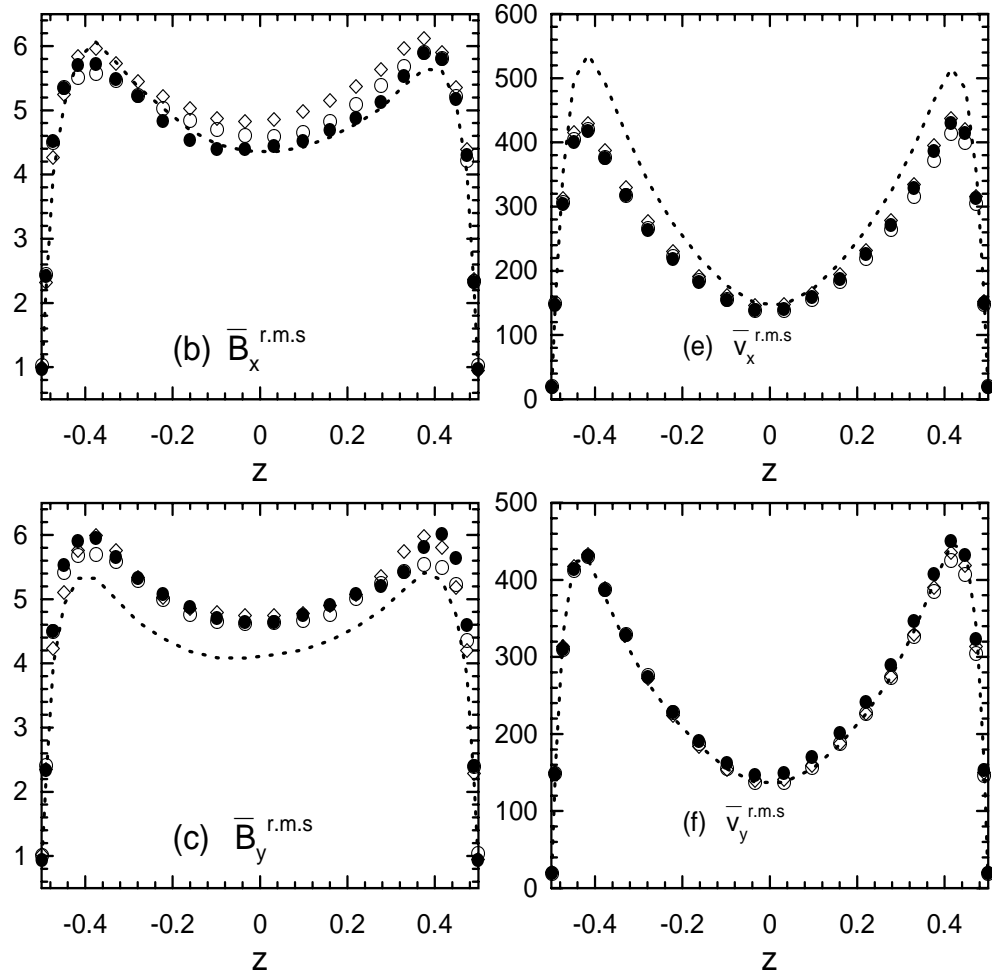


Figure 14. Vertical profiles of the time-averaged *r.m.s.* magnetic field components: (a) $\bar{B}_z^{r.m.s.}$; (b) $\bar{B}_x^{r.m.s.}$; (c) $\bar{B}_y^{r.m.s.}$; and of the time-averaged *r.m.s.* velocity components: (d) $\bar{v}_z^{r.m.s.}$; (e) $\bar{v}_x^{r.m.s.}$; (f) $\bar{v}_y^{r.m.s.}$: filtered DNS(H); \diamond : DNS(L). $\hat{\lambda} = 2\lambda$ for both the dynamic models.

Finally, the four different methods are evaluated in terms of the relative time spent, memory and storage required. As shown in Table 2, the application of the constant- C similarity model is only slightly expensive than the DNS(L) simulation. Among all the low resolution simulations, the dynamic similarity model is the most expensive, however is still cheap compared to the high resolution DNS models.

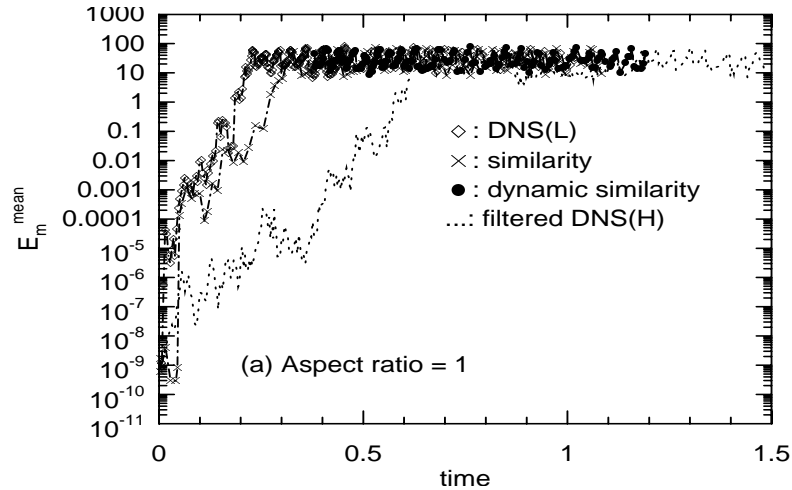
	DNS(L)	Constant -C similarity	Dynamic similarity	DNS(H)
<i>Elapsed real time</i>	1.00	1.34	2.12	3.83
<i>Memory</i>	1.00	1.13	1.17	2.74
<i>Storage</i>	1.00	1.00	1.00	3.88

Table 2: Performance of various models. Measured quantities are normalized by those from the DNS(L) simulation.

4 Effects of aspect ratio

So far the results and discussions are only for the plane layer with an aspect ratio $L/W = 1$. However, the Earth’s outer core has a much larger aspect ratio. Certainly, applicability of the subgrid-scale models in a larger aspect ratio geometry is crucial. Here we attempt to address this issue by carrying simulations with an aspect ratio 2. The same working parameters are used as in the unit aspect ratio case for comparison. Both cases have the same depth d . The larger aspect ratio case, therefore, has a larger volume than the smaller aspect ratio case. The high resolution simulation “DNS(H)” has been carried out on a grid with $64 \times 64 \times 32$, a resolution slightly larger than that of the unit aspect ratio case. The similarity model and the dynamic similarity models are applied to a $32 \times 32 \times 32$ grid. All three magnetic convection calculations start from the same initial condition which is from the same well-resolved and fully-developed nonmagnetic convection calculation. A low resolution simulation without any model “DNS(L)???” is also carried out on a $32 \times 32 \times 32$ grid (A “???” marks a unstable calculation). In all the simulations, time step is flexible and controlled by flow condition. For the “DNS(H)” calculation, the time step Δt can increase from 1.25×10^{-7} to 2×10^{-6} if the calculation is stable over 400 time steps. For the dynamic similarity model and the similarity model, the simulations are very stable and much larger time steps are allowed over a much shorter time interval (100 time steps)! The time step Δt is in the range $[5 \times 10^{-7}, 2 \times 10^{-6}]$. However, the “DNS(L)???” calculation suffered

great numerical instability. Its time step requirement is even stricter than the “DNS(H)”. The calculations were forced to stop at either the same time step used in the SGS model calculations or even in the “DNS(H)” calculations. This phenomenon did not occur in the aspect ratio 1 case, however it happens quite often in traditional turbulent LES simulations for very large Reynolds number flows. After several experimentations, the “DNS(L)???” calculation seemed to settle down at a time step between 5×10^{-8} and 2.5×10^{-7} over 400 time steps. As shown in Fig. 15 (b)(c), among all the calculations the dynamic similarity model simulation saturates the earliest. The “DNS(L)???” one saturates slightly earlier than the “DNS(H)”, which cannot be regarded as a convergent test because the numerical instability was mentioned above and the flow statistics will be shown below. A notable difference in the aspect ratio 1 case is that there the “DNS(L)” is very stable and it saturates the fastest. The reason for this difference is simply because for the aspect ratio 2, more fluids are convecting than in the aspect ratio 1 and presumably the convection is more vigorous and turbulent so that it requires much shorter time step and finer grid. The vigor of the convection in the aspect ratio 2 can be seen in Fig. 15(a) and (c) where the “DNS(H)” starts to saturates earlier at $t \approx 0.5$ than $t \approx 0.6 - 0.7$ in the aspect ratio 1, more than 10% shorter in terms of magnetic diffusion time.



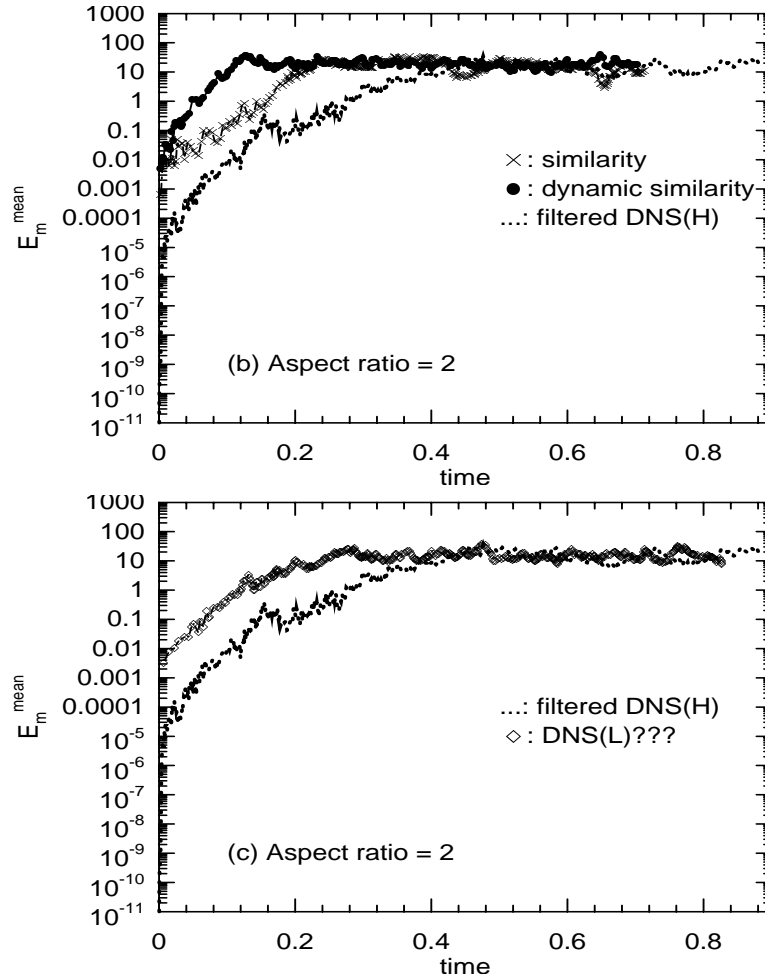


Figure 15. The growth of the mean magnetic field from different calculations at different aspect ratios. (a) Aspect ratio 1; (b) aspect ratio 2. Comparisons between SGS models and the high resolution calculations; (c) also aspect ratio 2. Comparison between the unstable low resolution calculation and the high resolution calculation. ? in the figure denotes a unstable calculation

As in the smaller aspect ratio geometry, the dynamic similarity model is less dissipative than the similarity model only in the larger wave numbers. Fig. 16, 17 and 18 show that results from the dynamic model are much closer to that from the “DNS(H)” than from the Constant $-C$ similarity model.

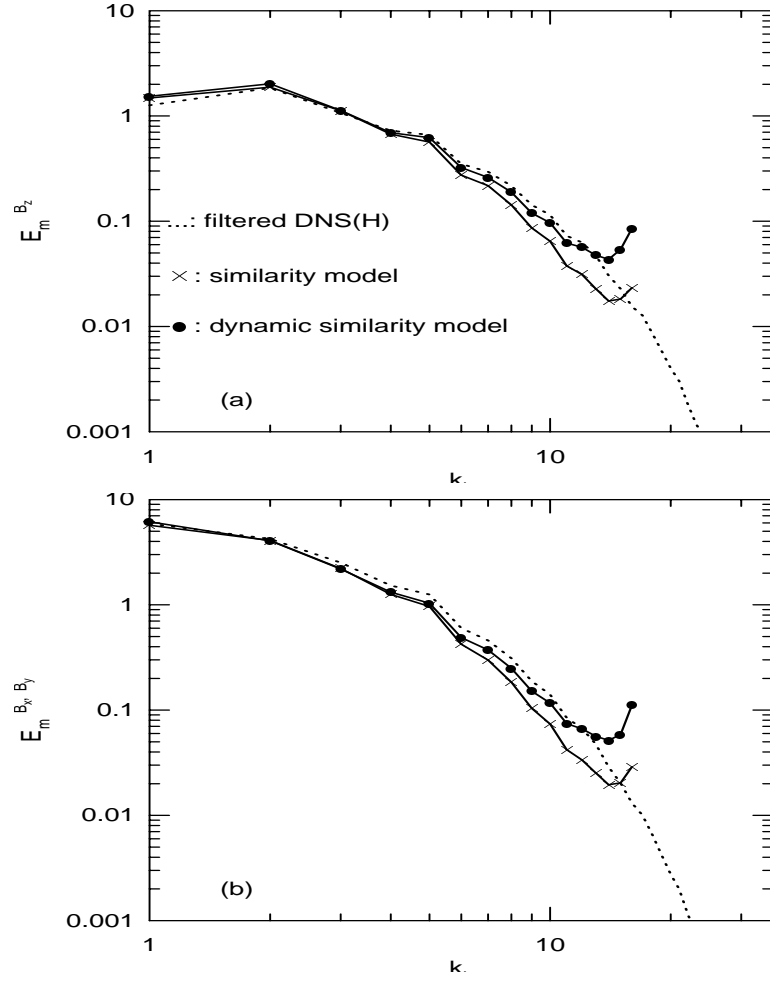


Figure 16. Time and vertically averaged spectra for (a) the transverse magnetic energy E_m^\perp ; (b) the longitudinal magnetic energy E_m^\parallel . \times : the *similarity* model with $\lambda = 2\Delta$ and $\Delta = 1/32$; \bullet : the *dynamic similarity* model with $\hat{\lambda}/\lambda = \lambda/\Delta = 2$ and $\Delta = 1/32$.

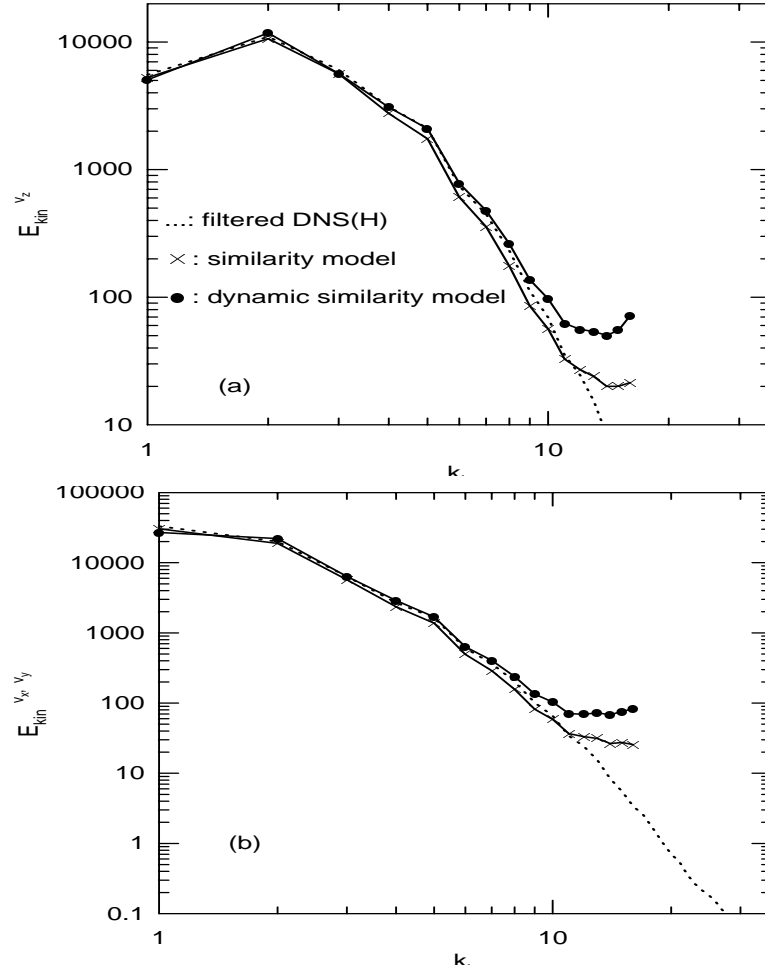


Figure 17. Time and vertically averaged spectra for (a) the transverse kinetic energy E_{kin}^{\perp} ; (b) the longitudinal kinetic energy E_{kin}^{\parallel} . \times : the *similarity* model with $\lambda = 2\Delta$; \bullet : the *dynamic similarity* model with $\hat{\lambda}/\lambda = \lambda/\Delta = 2$.

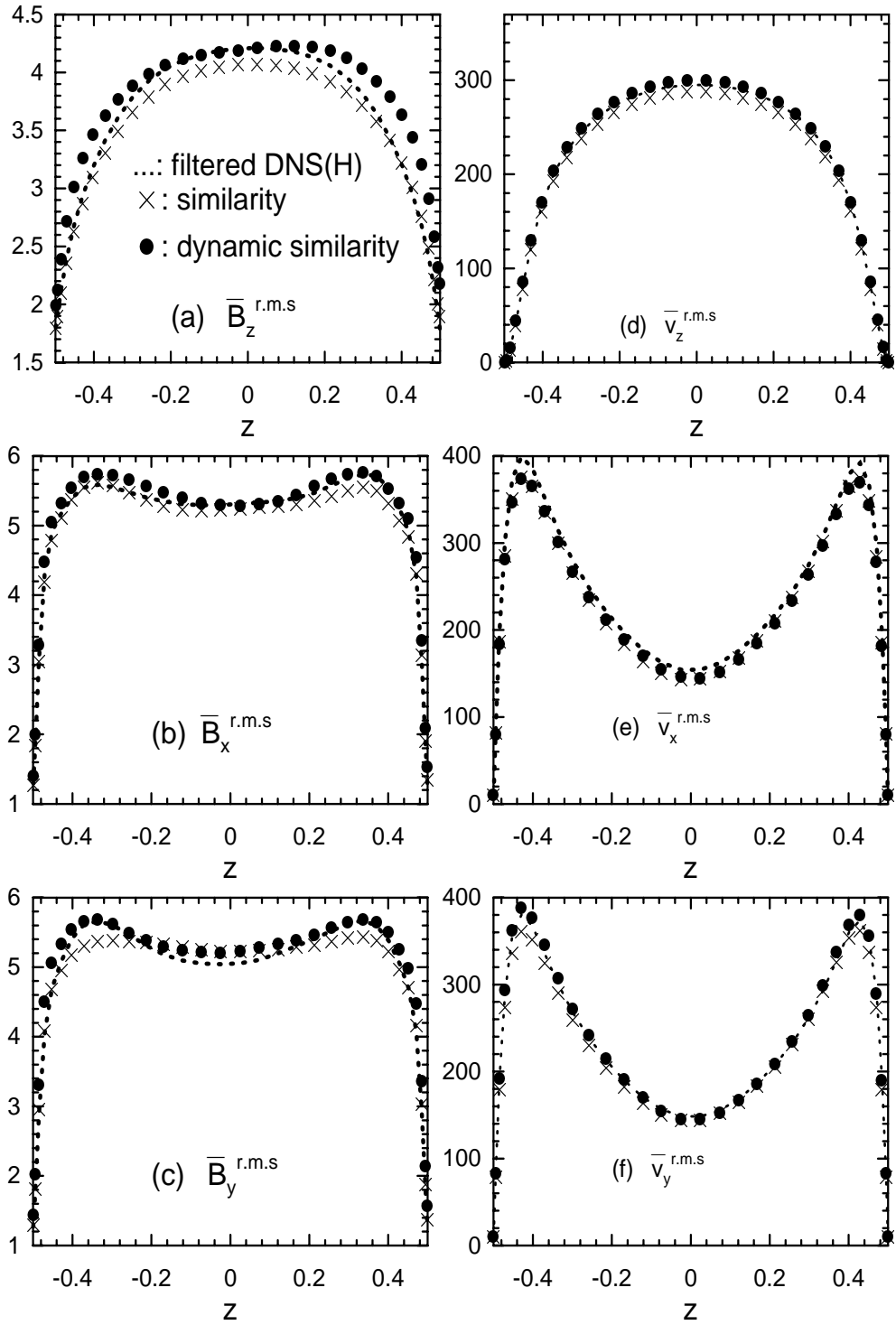
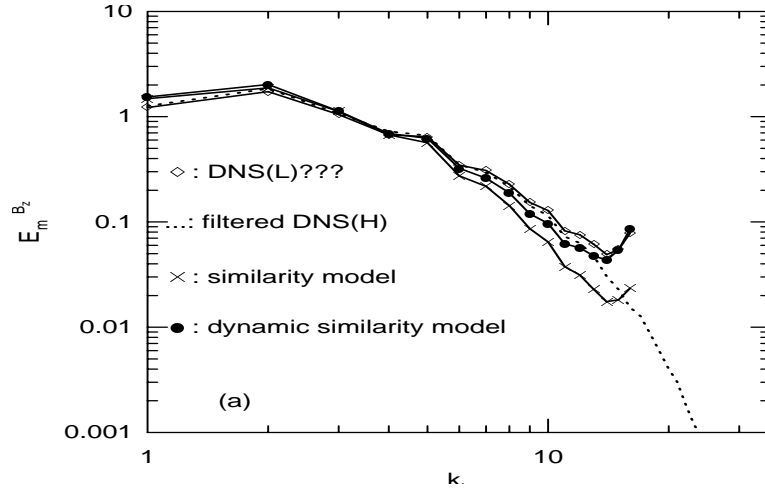


Figure 18. Vertical profiles of the time-averaged *r.m.s.* magnetic field components: (a) $\bar{B}_z^{r.m.s.}$; (b) $\bar{B}_x^{r.m.s.}$; (c) $\bar{B}_y^{r.m.s.}$; and the time-averaged *r.m.s.* velocity components: (d) $\bar{v}_z^{r.m.s.}$; (e) $\bar{v}_x^{r.m.s.}$; (f) $\bar{v}_y^{r.m.s.}$.

Regardless that the “DNS(L)???” simulation needs greater care (unstable) and is more time-consuming (smaller time step, longer to saturate), we compare its flow statistics with other calculations to have a complete assessment. Fig. 19 (a) certainly shows that the “DNS(L)???” data has the best fit with the “DNS(H)” from the transverse magnetic energy spectra among others. While Fig. 19 (b) shows that it has too high energy in $k_h = 1$ and larger wave numbers $k_h \geq 4$ from the kinetic energy spectra. Although in the smaller aspect ratio case, each time step spent on a low resolution direct calculation is smaller than other model calculations from Table 2, this table is not suitable for the aspect ratio 2 because the low resolution calculation is actually more expensive since the time step from “DNS(L)???” is much smaller and it takes longer time to saturate with frequent numerical instability. With all the factors taken account, no doubt the dynamic similarity model is the best bet.



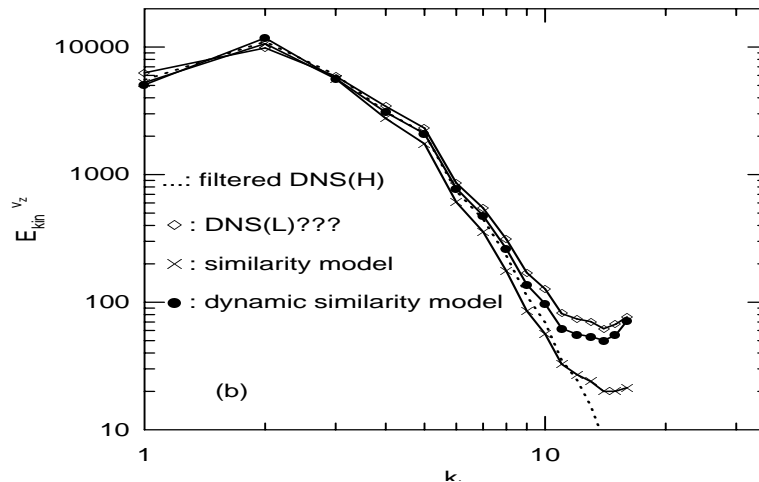


Figure 19. Comparison between the unstable “DNS(L)” simulation with other simulations for aspect ratio 2. Time and vertically averaged spectra for (a) the transverse magnetic energy E_m^\perp ; (b) the transverse kinetic energy E_{kin}^\perp .

5 Concluding Remarks

Modelling small-scale processes in the Earth’s outer core is regarded as one of the most difficult problems in the geodynamo simulations. The purpose of the present paper, is to study the performance of some well-established turbulent models in the environment of dynamo simulations. Strong nonlinearities are inherent in a rotating convection-driven dynamo, which certainly will bring great difficulties to a turbulent model. Therefore, our first step is to test these models in a very simple plane layer geometry which nevertheless does not lack of basic elements in a dynamo simulation, such as nonlinearity, rotation and self-sustained magnetic field.

In this study, we have investigated for the first time similarity models in a convection-driven dynamo simulation. The calculations presented here have demonstrated that the similarity model and the dynamic similarity model describe convection-driven dynamos at high magnetic Reynolds number successfully. In particular, the models are numerically stable. The agreement between the LES and high resolution DNS data is impressive. The models produce not only

quite reasonable magnetic and kinetic energies at large scales, but also comparable magnetic and velocity field fluctuations in the center region of the fluid layer.

The sensitivity of the results to the filter type has been studied by Buffett (2003) in an *a priori* test and it should be attempted in a LES in the future. Only Gaussian filters were used here, but the effect of varying the filter width was investigated. Although the choice of $\lambda = 4\Delta/3$ is found to yield the best result, the *a priori* tests directly comparing the subgrid scale terms gave excellent agreement between the spatial distribution derived using the similarity model and that derived from direct computation. This gives strong support to the basic idea of the similarity model, that the form of the SGS terms can be predicted from the modes at slightly larger scales. Although the amplitude showed considerable variation with filter width, the LES simulations with the constant C similarity model nevertheless gave reasonable results and the results were much less sensitive to the choice of filtering scale compared with the *a priori* tests. The dynamic similarity model involves two levels of filtering and avoids the necessity of arbitrarily choosing the C constants. The improvement of the dynamic similarity model over the original, constant- C similarity models is evident only when the two filtering scales are properly chosen. Unless the scales are well chosen, the dynamic similarity model does not justify its greater computational expense.

The effect of aspect ratio on the performance of the SGS models is also investigated by carrying out simulations with aspect ratio 1 and 2. The dissipative nature of the dynamic similarity and the constant- C similarity models allows the models to be able to take larger time step without the expense of numerical stability. Instead, the low resolution direct simulation frequently encounters numerical instability and has to resort to much smaller integration time step. Considering both the time cost and flow statistics, we find that the dynamic similarity model is still the best choice. The results from both the aspect ratio 1 and 2 have confirmed that the model performances are not influenced by the aspect ratio chosen, although one may argue that aspect ratio 2 is still too much smaller than that of the Earth's outer core. Indeed, it is very important to study systematically what is the largest aspect ratio these models can still

be applicable to and in what parameter range. However, it is beyond present scope of study.

It should be recognized that the models still fail to produce enough dissipation at very small scales. Slightly greater magnetic energies can also be observed at larger scales for different aspect ratios; see Figs. 9 (a), 13(a) and 16 (a). Will this become a serious problem when the magnetic Reynolds number increases ($Re_m \gg 100$ perhaps)? It should be also recognized that this study is only carried on a system with an infinite Pr number. Although presently we are only interested in the long time scales, we can't predict what will be the outcomes of these SGS models for a finite Pr system. For a very small Pr number (or large magnetic Ekman number), the fluid inertia is much more important than the Maxwell stress such that the SGS term in the momentum equation is recovered to the traditional Reynolds stress. Many intensive studies on the modelling of the Reynolds stress can be found in the classic turbulent flows, which may be helpful for a small Pr number situation. All these questions present significant and exciting challenges for future research.

Acknowledgments. We thank Gary Glatzmaier, Pablo Mininni and Paul Roberts for helpful suggestions and stimulating discussions. We also thank the referees for the valuable suggestions. The simulations were carried out on the Beowulf cluster at UC Santa Cruz, which is supported by an NSF MRI grant. This research was also supported by NSF grant EAR-0222334.

References

- [1] Bardina, J., Ferziger, J.H. & Reynolds, W.C., 1980. Improved subgrid scale models for large-eddy simulations, *Am. Inst. Aeronaut. Astronaut. Paper*, 80-1357.
- [2] Braginsky, S.I. & Meytlis, V.P., 1990. Local turbulence in the Earth's core, *Geophys. Astrophys. Fluid Dynam.*, **55**, 71–87.
- [3] Buffett, B.A., 2003. A comparison of subgrid-scale models for large-eddy simulations of convection in the Earth's core, *Geophys. J. Internat.*, **153**, 753–765.

- [4] Busse, F.H., Grote, E. & Tilgner, A., 1998. On convection driven dynamos in rotating spherical shells, *Stud. Geophys. Geod.*, **42**, 1–6.
- [5] Chen, Q., Chen, S., Eyink, G.L., & Holm, D.D., 2005. Resonant interactions in rotating homogeneous three-dimensional turbulence, *J. Fluid Mech.*, **542**, 139–164.
- [6] Chen, Q. & Glatzmaier, G.A., 2005. Large eddy simulations of two-dimensional turbulent convection in a density-stratified fluid, *Geophys. Astrophys. Fluid Dynam.*, **99**, 355–375.
- [7] Childress, S. & Soward, A.M., 1972. Convection driven hydromagnetic dynamo, *Phys. Rev. Lett.*, **29**, 837–839.
- [8] Christensen, U.R., Olson, P. & Glatzmaier, G.A., 1999. Numerical modelling of the geodynamo: a systematic parameter study. *Geophys. J. Internat.*, **138**, 393–409.
- [9] Donald, J.T., & Roberts, P.H., 2004. The effect of anisotropic heat transport in the Earth’s core on the geodynamo, *Geophys. Astrophys. Fluid Dynam.*, **98**, 367–384.
- [10] Frisch, U., Pouquet, A., Liorat, J. & Mazure, A., 1975. Possibility of an inverse cascade of magnetic helicity in magnetohydrodynamic turbulence, *J. Fluid Mech.*, **68**, 769–778.
- [11] Leonard, A., 1974. Energy cascade in large-eddy simulations of turbulent flow, *Adv. Geophys.*, **18**, 237–248.
- [12] Germano, M., 1986. A proposal for a redefinition of the turbulent stresses in the filtered Navier-Stokes equations, *Phys. Fluids*, **29**, 2323–2324.
- [13] Germano, M., Piomelli, U., Moin, P. & Cabot, W.H., 1991. A dynamic subgrid-scale eddy viscosity model, *Phys. Fluids A*, **3**, 1760–1765.
- [14] Glatzmaier, G.A. & Roberts, P.H., 1995. A three-dimensional convective dynamo solution with rotating and finitely conducting inner core and mantle, *Phys. Earth Planet. Inter.*, **91**, 63–75.

- [15] Fautrelle, Y. & Childress, S., 1982. Convective dynamos with intermediate and strong fields, *Geophys. Astrophys. Fluid Dynam.*, **22**, 235–279.
- [16] Jones, C.A. & Roberts, P.H., 2000. Convection-driven dynamos in a rotating plane layer, *J. Fluid Mech.*, **404**, 311–343.
- [17] Jones, C.A. & Roberts, P.H., 2005. Turbulence models and plane layer dynamos, In *Fluid Dynamics and Dynamos in Astrophysics and Geophysics* (ed. A.M. Soward, C.A. Jones, D.W. Hughes & N.O. Weiss), pp. 295–330, *CRC Press, Baton Rouge*.
- [18] Kageyama, A., Sato, T., Watanabe, K., Horiuchi, R., Hayashi, T., Todo, Y., Watanabe, T.H., & Takamaru, H., 1995. Computer simulation of a magnetohydrodynamic dynamo, *Phys. Plasma.*, **2**, 1421–1431.
- [19] Kida, S., Araki, K. & Kitauchi, H., 1997. Periodic reversals of magnetic field generated by thermal convection in a rotating spherical shell, *J. Phys. Soc. Jpn.*, **66**, 2194–2201.
- [20] Kuang, W. & Bloxham, J., 1997. An Earth-like numerical dynamo model, *Nature*, **389**, 371–374.
- [21] Lilly, D.K., 1992. Proposed modification of the Germano subgrid-scale closure method, *Phys. Fluids A*, **14**, 633–635.
- [22] Matsui, H. & Buffett, B.A., 2005. Sub-grid scale model for convection-driven dynamo in a rotating plane layer, *Phys. Earth Planet. Inter.*, **153**, 108–123.
- [23] Meneguzzi, M. & Pouquet, A., 1989. Turbulent dynamos driven by convection, *J. Fluid Mech.*, **35**, 319–340.
- [24] Meneveau, C. & Katz, J., 2000. Scale-invariance and turbulence models for large-eddy simulation, *Annu. Rev. Fluid Mech.*, **32**, 1–32.

- [25] Phillips, C.G. & Ivers, D.J., 2001. Special interactions of rapidly-rotating anisotropic turbulent viscous and thermal diffusion in the Earth's core, *Phys Earth Planet. Inter.*, **128**, 93–107.
- [26] Phillips, C.G. & Ivers, D.J., 2003. Strong field anisotropic diffusion models for the Earth's core, *Phys. Earth Planet. Inter.*, **140**, 13–28.
- [27] Pierre, M.St., 1994. The strong field branch of the Childress-Soward dynamo, In *Stellar and Planetary Dynamos* (ed. M. R. E. Proctor & A. D. Gilbert), pp. 295–302, *Cambridge University Press*.
- [28] Piomelli, U., 1993. High Reynolds number calculations using the dynamic subgrid-scale model, *Phys. Fluids A*, **5**, 1484–1490.
- [29] Pouquet, A., Frisch, U. & Leorat, J., 1976. Strong MHD helical turbulence and nonlinear dynamo effect, *J. Fluid Mech.*, **77**, 321–354.
- [30] Rotvig, J. & Jones, C.A., 2002. Rotating convection-driven dynamos at low Ekman number, *Phys. Rev. E*, **66**, 056308.
- [31] Sakuraba, A. & Kono, M., 1997. Effects of the inner core on the numerical simulation of the magnetohydrodynamic dynamo, *Phys. Earth Planet. Inter.*, **11**, 105–121.
- [32] Shimizu, H. & Loper, D.E., 1997. Time and length scales of buoyancy-driven flow structures in a rotating hydromagnetic fluid. *Phys. Earth Planet. Inter.*, **104**, 307–329.
- [33] Soward, A.M., 1974. A convection driven dynamo I. The weak field case. *Phil. Trans. R. Soc. Lond. A*, **275**, 661–651.
- [34] Wong, V.C. & Lilly, D.K., 1994. A comparison of two dynamic subgrid closure methods for turbulent thermal convection, *Phys. Fluids*, **6**, 1016–1023.